Data acquisition and imaging using wavelet transform: a new path for high speed transient force microscopy

Nanoscale Advances

Accepted Manuscript

Data acquisition and imaging using wavelet transform: a new path for high speed transient force microscopy

View Article Online
DOI: 10.1039/D0NA00531B

Amir Farokh Payam, Pardis Biglarbeigi*, Alessio Morelli, Patrick Lemoine, James McLaughlin, Dewar Finlay*

Nanotechnology and Integrated Bioengineering Centre (NIBEC), School of Engineering, Ulster University, Jordanstown Shore Road, BT37 0QB, Northern Ireland, United Kingdom

E-mail: a.farokh-payam@ulster.ac.uk

Keywords: Atomic Force Microscopy, Continuous Wavelet Transform, Transient Response, Amplitude and Phase Images.

The unique ability of Atomic Force Microscopy (AFM) to image, manipulate and characterize materials at nanoscale has made it remarkable tool in nanotechnology. In dynamic AFM, acquisition and processing of the photodetector signal originating from probe-sample interaction is a critical step in data analysis and measurements. However, details of such interaction including its nonlinearity and dynamics of the sample surface are limited due to the ultimately bounded bandwidth and limited time scales of data processing electronics of standard AFM. Similarly, transient details of the AFM probe's cantilever signal are lost due to averaging of data by techniques which correlate the frequency spectrum of the captured data with a temporally invariant physical system. Here, we introduce a fundamentally new approach for dynamic AFM data acquisition and imaging based on applying the wavelet transform on the data stream from the photodetector. This approach provides the opportunity for exploration of the transient response of the cantilever, analysis and imaging of the dynamics of amplitude and phase of the signals captured from the photodetector. Furthermore, it can be used for the control of AFM which would yield increased imaging speed. Hence the proposed method opens a pathway for high-speed transient force microscopy.

View Article Online
DOI: 10.1039/D0NA00531B

1. Introduction

Atomic force microscopy is a versatile instrument for imaging and characterization of electrical, mechanical, physical and chemical properties of materials at nanometer scale with atomic resolution [1]–[9]. The AFM working principle is based on the interaction between the cantilever probe system and the surface, and particularly in amplitude modulation AFM – one of the most used AFM modes - such interaction is sensed by vibrating the probe's cantilever near resonance. Vibration information, especially the amplitude which is used by the feedback system to follow the surface, are embedded in the cantilever-tip motion signal that is detected by a photodiode detector. The data stream from the photodetector is processed via a data acquisition and processing system that explores the information on local properties and structure [3], [9]–[12]. The exceptional capability of AFM to image, characterize and manipulate materials in different environments including vacuum, air and liquid with remarkable signal to noise ratio triggered the development of advanced AFM techniques. In the three decades after its invention, much attention has been focused on the development of low noise platforms, high quality and fast cantilever probes, improvement of nano-positioning speed, measurement precision and bandwidth [13], [14], [23]–[27], [15]–[22]. Despite remarkable improvements in the increasing speed of AFM which has led to the development of High-Speed AFM [28], relatively little effort has been devoted to improvements in information transfer, high-speed amplitude detection and transient dynamics of the cantilever during interaction with the sample under evaluation. The conventional method for amplitude calculation during AFM operation relies on the use of the lock-in amplifier (LIA) [29]–[31], which is not suitable for high-speed operation. The main limitation of LIA in calculation of amplitude for the high-speed operation is the low pass filter which not only limits the bandwidth but also results in loss of information in transient responses. In order to further improve measurement speed, methods alternative to LIA such as peak-hold method [32], Fourier analysis [33], real-time integration [34], [35], Lyapunov estimation [36] and Kalman filter approach [37] have been proposed. However, although these methods can speed up the process of amplitude estimation, the dynamic information of cantilever interaction is strictly limited to only several measured parameters. Although for linear systems this mechanism is acceptable, complex multidimensional cases - such as non-linearities, multifrequency, couplings of modes and transient response - cannot be solved thoroughly. All these cases carry information about the material's properties that cannot be skipped or effectively squeezed [10].

View Article Online
DOI: 10.1039/D0NA00531B

Recording the amplitude and phase response of the cantilever with respect to the real time for different harmonics and frequencies in both transient and steady state regimes can lead to an increase of the speed and precision of feedback control. Together, with development of advanced multifrequency techniques, this would result in the possibility to extract more detailed information from the tip-sample interaction - especially in cases where the dynamic response of the sample is relevant - and explore sample properties and structures during imaging in more detail. This opens the possibility for transient force microscopy which would record the information conveyed by the sensing tip as a transient motion of the cantilever, in contrast to steady state operation used in standard dynamic techniques [38]–[44]. In the steady state analysis, in addition to the display of the images based on the averaging of the data per pixel, spectral analysis provided by standard techniques, such as Fourier transform (FT), provides an averaged spectrum which is integrated over the whole acquisition time [41]–[44]. So, in order to analyze the whole dynamics of the non-stationary signals from the photodetector, an approach that is capable to combine time domain and frequency domain analysis is mandatory. The wavelet transform (WT) method surpasses the imposed constrains by using the wavelet as the basis function [45]. In using the WT, not only the steady state response of cantilever can be detected, but also the whole dynamics - including transient and higher frequency responses - are captured and recorded. Previously, the WT has been used in the AFM for the analysis of scanned images [46], eigenmodes and energy dissipation for force spectroscopy [43], [44], [47]–[51], [52], characterization of passive micro rheology of living myoblasts [53] and investigation of the amplitude of higher harmonics in tapping mode AFM [41], [42].

View Article Online
DOI: 10.1039/D0NA00531B

In this paper, for the first time, wavelet theory is used to analyze the multidimensional dynamic of both amplitude and phase of the cantilever signal acquired during imaging. The captured data are used to explore the probe-sample interaction and use the transient dynamic to provide amplitude and phase images of the sample. Working on simulated data, we demonstrate that this method is effective in detecting transient response in relation to samples properties variation in different environmental conditions. Finally, by applying the WT on the data stream from AFM photodetector, the resulting amplitude and phase images are shown to be in agreement – and indeed surpassing in resolution – with the ones obtained by lock-in techniques embedded in the AFM system used for the experiments.

This could be a breakthrough in the development of AFM technology towards detection of the whole dynamic response of amplitude and phase of the cantilever. It would give the ability to capture images in both transient and steady state regimes and provide the opportunity for full acquisition of cantilever data during experiments while in current lock-in amplifier based AFM systems only the steady state values of amplitude and phase are extracted and averaged to provide the corresponding images and control the AFM. The real time implementation of the proposed technique can significantly improve the speed of AFM operation and capability of multifrequency methods. Using the detected real time amplitude in the imaging and control of AFM which requires the use of application specific hardware (e.g. FPGA [54]) to achieve the levels of performance necessary, can lead to the new concept in the AFM technology of high-speed transient force microscopy.

2. Wavelet Transform Method

The Wavelet transform (WT) can transform a time domain signal into a representation that can illustrate the signal information more concisely whilst also highlighting information that was not apparent in the original signal. The WT is defined as the convolution of a signal, $x(t)$, and a localized wavelike function, $\Psi(t)$, also known as the mother wavelet. Mother wavelets have finite energy and should follow the admissibility condition, which states that the wavelet has no zero-frequency component, and therefore the mother wavelet has a zero mean. The WT is then obtained by local matching of the translated and dilated mother wavelet with the signal [55].

The Continuous Wavelet Transform (CWT) is the sliding convolution of a signal, $x(t)$, and the mother wavelet, $\Psi(t)$, defined as Equation (1).

View Article Online
DOI: 10.1039/D0NA00531B

$$W(t,s) = \frac{1}{s}\int x(u)\Psi^*\left(\frac{u-t}{s}\right)du \qquad (1)$$

Where s and t are the scale and time shift of the mother wavelet, Ψ, respectively and Ψ^* denotes the complex conjugate of Ψ . The daughter wavelet, $W(t,s)$, is the wavelet coefficient of the signal localized in (t,s). Therefore, the CWT presents a time-scale analysis which characterizes the power of different scales against time. The plot that can be generated using the magnitude of daughter wavelet coefficients can represent the spectral energy of the signal and is called scalogram [56].

The CWT uses scales as an alternative to frequency and decomposes a signal into a time-scale plane and each scale contains a range of frequencies. The transform of the signal into each scale is performed by a wavelet band-pass filter localized in frequency, ω_s. The relative frequency, $\Delta\omega_s/\omega_s$, is constant for all the scales. Therefore, in lower frequencies longer wavelets are considered to improve the frequency localization, while in higher frequencies shorter wavelets are used to recover a better time localization. Therefore, the temporal length or the time shift of the wavelet is variable depending on the scale or the frequency range [57]. However, this implies that since CWT is not completely localized in time, it suffers from edge artifact [58].

The number of scales is determined by the number of voices and octaves, where octave is defined as the frequency range and voices per octave are the number of scales across each octave [59]. In this study, voices per octave are 40 for all the CWT calculations.

There are numerous kinds of mother wavelets. In this study, we used Generalized Morse Wavelet (GMW). GMWs are useful in analyzing modulated signals [60] and are defined by complex analytic wavelet transform that can reserve the information of both amplitude and phase. GMWs use a two-parameter family of wavelets, namely symmetry, γ, which determines the wavelet shape and compactness parameter, β. GMWs in frequency-domain can be defined as Equation (2) [61]:

$$\Psi_{(\beta,\gamma)} = \int_{-\infty}^{\infty} \psi_{\beta,\gamma}(t) e^{-i\omega t} dt = U(\omega) a_{\beta,\gamma} \omega^{\beta} e^{-\omega^{\gamma}} \quad (2)$$

View Article Online
DOI: 10.1039/D0NA00531B

where $a_{\beta,\gamma}$ defines a normalization constant and $U(\omega)$ is the unit step function. By changing β and γ , GMW is capable of reserving wide range of signal characterizations while remaining analytic [62]. Accordingly, one important variable that can be used in defining the behavior of GMWs is the time-bandwidth product which can be calculated by Equation (3).

$$P_{\beta,\gamma}^{2} = \beta\gamma \quad (3)$$

It has been shown that the number of oscillations that can fit into the time-domain wavelet is equal to $P_{\beta,\gamma}/\pi$ and $P_{\beta,\gamma}$represents the wavelet duration or inverse bandwidth. Therefore, defining an appropriate GMW as the mother wavelet depends on the value of $P_{\beta,\gamma}^{2}$ and γ. Different studies have identified that Airy wavelets, GMWs with shape parameter $\gamma = 3$, have a Gaussian characteristic with high symmetry and concentration of time and frequency [61], [63].

In this study, we used Airy wavelets with of $P_{\beta,\gamma}^{2} = 60$, where each time-domain wavelet can fit 2.5 oscillations.

Considering a normalized GMW, the magnitude of the complex CWT coefficients is equivalent to the amplitude, Equation (4) and phase of the complex value corresponds to the time-related characteristic of the signal, Equation (5).

$$|W(a,b)| = \sqrt{\Re(W(a,b))^2 + \Im(W(a,b))^2} \quad (4)$$

$$\angle W(a,b) = arctan(\frac{\Im(W(a,b))}{\Re(W(a,b))}) \quad (5)$$

Where $\Re$ and $\Im$ are the real and the imaginary part of the complex CWT coefficient, respectively. Equation (5) defines the phase of the complex coefficient, however, in order to find the local phase response of the cantilever, its signal should be compared to the drive signal of the cantilever.

The Cross Wavelet Transform (XWT) calculates the interaction between two time-series signal and is defined as Equation (6).

$$W_{xy}(a,b) = W_x(a,b).\,W_y{}^*(a,b) \tag{6}$$

View Article Online
DOI: 10.1039/D0NA00531B

Where x and y are the two time-series signals (i.e. cantilever and drive signal), W is the CWT coefficient of the signals localized at (a,b) and W^* denotes the complex conjugate of the CWT coefficient [64]. $W_{xy}(a,b)$ argument can define the local relative phase between the cantilever and the drive signal of the cantilever.

A slow varying phase lag can be computed between two signals if they are physically related. Mathematically, wavelet coherence can give information on local correlation of two time-series [65]. Therefore, local phase lag between the two time-series signals using XWT is only valid at the CWT scales that the two daughter wavelets are coherent.

Wavelet Coherency determines the coherence of XWT in a time-frequency plane and can be calculated by Equation (7).

$$R^2(a,b) = \frac{\langle W_{xy}(a,b)\rangle^2}{|\langle W_x(a,b)\rangle|^2.\,|\langle W_y(a,b)\rangle|^2} \tag{7}$$

Where $\langle . \rangle$ denotes the smoothing operator in time and frequency [65], [66]. As shown in Equation (7), wavelet coherence can be regarded as a localized correlation coefficient in time-frequency plane. Wavelet coherence values are in the range of [0,1], with values closer to one showing a higher correlation between the two signals.

3. Materials & Methods

3.1. Simulation

For simulations, the cantilever-tip motion in dynamic AFM (hence the signal from the photodetector) is described as a driven and dampen point-mass oscillator that is under the influence of conservative and non-conservative forces [40] and numerical solutions are calculated using a fourth order Runge-Kutta algorithm in C++ software. The equation is described by:

$$\ddot{z}_i + \frac{\omega_i}{Q_i}\dot{z}_i + \omega_i^2 z_i = \frac{\omega_i^2 F_{di}}{k_i} + \frac{\omega_i^2 F_{ts}}{k_i} \tag{8}$$

View Article Online
DOI: 10.1039/D0NA00531B

Where subscripts $i = 1,2$ refer to the first and second flexural mode of cantilever, respectively. z_i, F_{di}, ω_i, Q_i and k_i are the tip deflection, drive force, natural frequencies, quality factors and spring constant of the cantilever, respectively. The interaction force is described by conservative and non-conservative viscoelastic force using following model [67]:

$$F_{tsc} = \begin{cases} -\frac{A_h R_t}{6d^2} & d \geq a_0 \\ -\frac{A_h R_t}{6d^2} + \frac{4E_{eff}\sqrt{R_t}}{3}(a_0 - d)^{\frac{3}{2}} & d < a_0 \end{cases} \tag{9}$$

$$F_{tsnc} = \begin{cases} 0 & d \geq a_0 \\ -\eta\sqrt{R_t(a_0 - d)}\dot{d} & d < a_0 \end{cases} \tag{10}$$

Where $A_h$is Hamaker constant, R_t is the tip radius, η is viscosity and $E_{eff} = \left[\frac{(1-\upsilon_s^2)}{E_s} + \frac{(1-\upsilon_t^2)}{E_t}\right]^{-1}$ is the effective Young-Modulus of the interaction, E_t, E_s, υ_t and υ_s are Young Moduli and Poisson's ratio of tip and sample, respectively. d is the minimum distance between tip and sample which is defined as:

$$d = z + z_0 + z_c \tag{11}$$

Where z_c is the average distance between cantilever base and sample surface and z_0 is the average tip deflection. For air environment simulations (considering only the first mode) free amplitude is 10 nm, frequency 300 kHz, cantilever spring constant $k = 30$ N/m, quality factor $Q = 300$ and tip radius $R_t = 10$ nm. For liquid environment simulations (first and second mode considered, due to the effect of second eigenmode [68], [69]) free amplitude is 13.5 nm, first and second natural frequencies 18.6 kHz and 170 kHz, respectively, tip radius (R_t) 10 nm, spring constants and quality factors of the first and second modes are $k_1 = 0.22$N/m, $k_2 = 12.23$ N/m, $Q_1 = 1.62$ and $Q_2 = 4.526$. While amplitude modulation AFM mapping works by keeping the average probe-sample distance constant by use of a feedback loop, all simulations in the present work are performed assuming no action from feedback and with varying distance (i.e. probe hovering above the surface without change in absolute Z height).

View Article Online
DOI: 10.1039/D0NA00531B

In this way topography variations will yield a clear transient signal, which would otherwise be depending on the speed of reaction of the feedback.

3.2. Experiments

Two samples with distinctly different features have been employed for the present work. The first one (sample 1) is an AFM calibration sample (PNI AFM reference, Pacific Nanotechnology) with patterns of square features with regular size and pitch. The sample is made of silicon nitride film deposited on a silicon substrate. The experiments on this sample were performed on the edge of a 5x5 μm^2 square feature. The second sample (sample 2) is a qualification sample (used to estimate the tip radius of curvature of employed AFM probes) displaying granular sharp nanostructure. The sample is made of a hard thin film coating deposited on a silicon chip (TipCheck sample from BudgetSensors.com). The experiments were performed in air using a commercial AFM system (D3100 Nasoscope III Digital Instruments, now Bruker) in amplitude modulation AFM (tapping mode) equipped with signal access module (SAMIII Digital Instruments) through which the signal from the photodetector could be intercepted. Real time cantilever vertical deflection signal was acquired via data acquisition board (NI USB-6366, DAQ Device, National Instruments, Austin, TX, USA). Images of 2 μm scan size and aspect ratio 10 (24x256 pixels) were acquired at a scan rate of 1 Hz, with a silicon probe for soft tapping mode (FMV-A Bruker, spring constant 2.8 N/m, resonance frequency 72.96 kHz), at a drive frequency of 72.95 kHz and set amplitude 85% that recorded at 100 nm lift from the surface. The same parameters were used to acquire a 2 μm image of the reference sample with aspect ratio 1 (128x128 pixels) at a scan rate of 4 Hz. Deflection sensitivity was calibrated after each set of experiment was calibrated by performing force curves on the qualification sample.

4. Results and Discussion

View Article Online
DOI: 10.1039/D0NA00531B

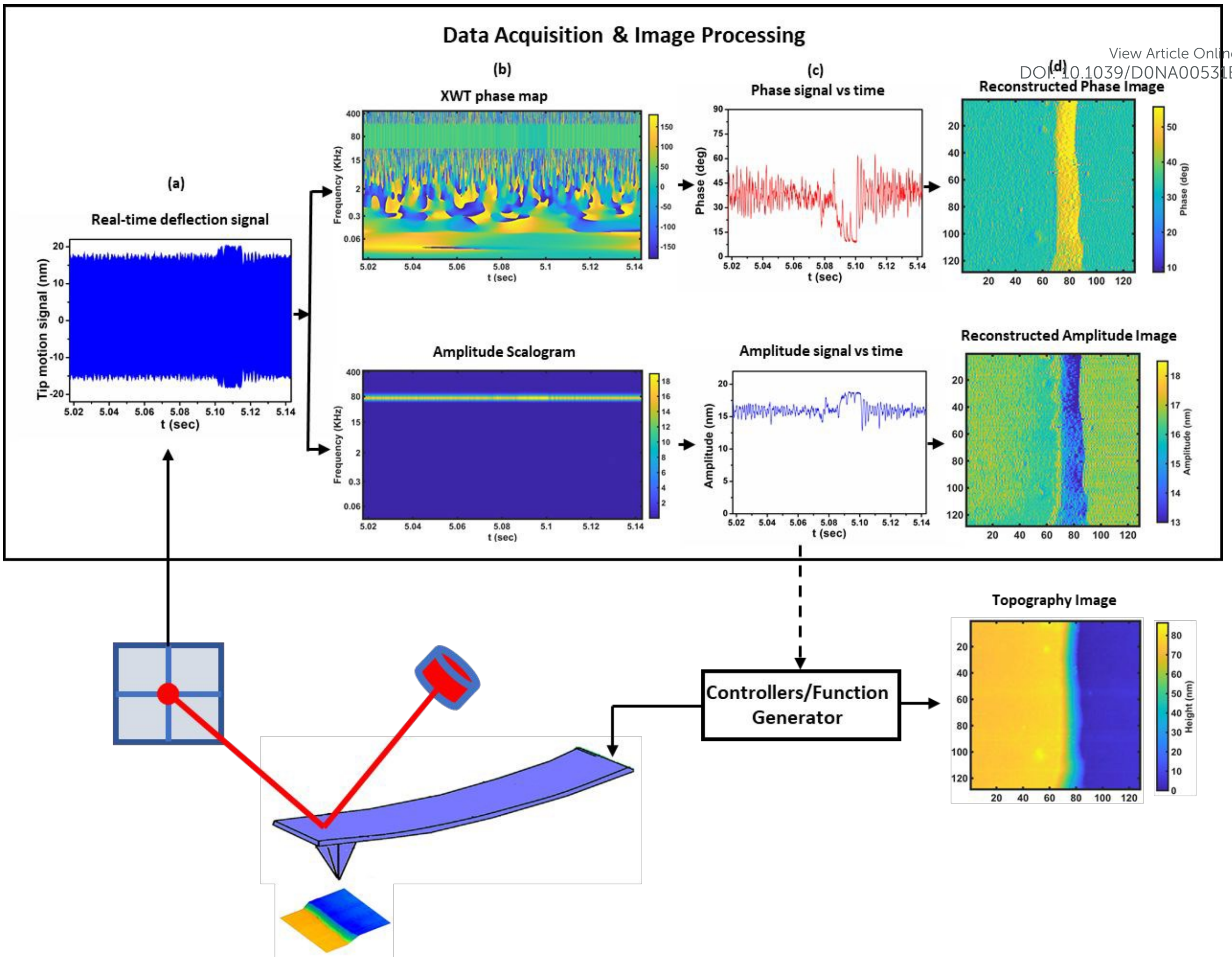

Figure 1. Schematic of the proposed method. Images collected over a single tapping mode scan with the feedback maintaining a set-point amplitude. a) The real-time signal acquired by photodetector. b) Scalogram and time-frequency phase map obtained via CWT using the raw signal from the photodetector. c) Temporal amplitude and phase versus time at each frequency extracted from the CWT maps. d) The amplitude and phase images reconstructed from the temporal signals of the cantilever.

The proposed wavelet transform method, as schematized in figure 1, is fed with the cantilever vertical deflection signal as tracked by the AFM photodetector (Figure 1-a). From this signal the CWT extracts the dynamics of amplitude (magnitude of the CWT coefficients) and phase (XWT) of cantilever motion with respect to time, which can be represented by scalogram and phase map as shown in Figure 1-b. In this way all the transient and steady state information of the two variables are available. From this collection of information both the transient and averaged amplitude and phase features can be extracted by selecting the data within the corresponding time interval at the frequency of interest (Figure 1-c). Finally, the images of amplitude and phase can be reconstructed from separated signals of phase and amplitude versus time (Figure 1-d).

View Article Online
DOI: 10.1039/D0NA00531B

Furthermore, by integrating such method within the AFM system itself, the extracted amplitude information could be used to control the AFM to keep the setpoint value. This would yield improvement in AFM measurements speed by substituting the lock-in amplifier which has a bandwidth limitation due to the low pass filter. For this purpose, the CWT can be implemented by FPGA to detect and calculate the phase and amplitude signals in real-time from photodetector signal and provide the amplitude signal as an input of the feedback controller. Integration of implementation of CWT by FPGA [70], [71] and recent development of FPGA for the control of high-speed AFM [54], [72] represent the applicability of the proposed method for high-speed operation.

In first place, we evaluate the effectiveness and performance of the continuous wavelet transform to provide the amplitude and phase of the signal versus time consisting of both transient and steady state regimes. For this purpose, a simulated cantilever deflection signal is converted using CWT and compared with a signal obtained from slow time varying function theory [67] (Figure 2), showing very good agreement. It is however worthy remarking that slow time varying method is only applicable for theoretical studies and cannot be applied experimentally, the main advantage of CWT being its ability to be employed in both cases.

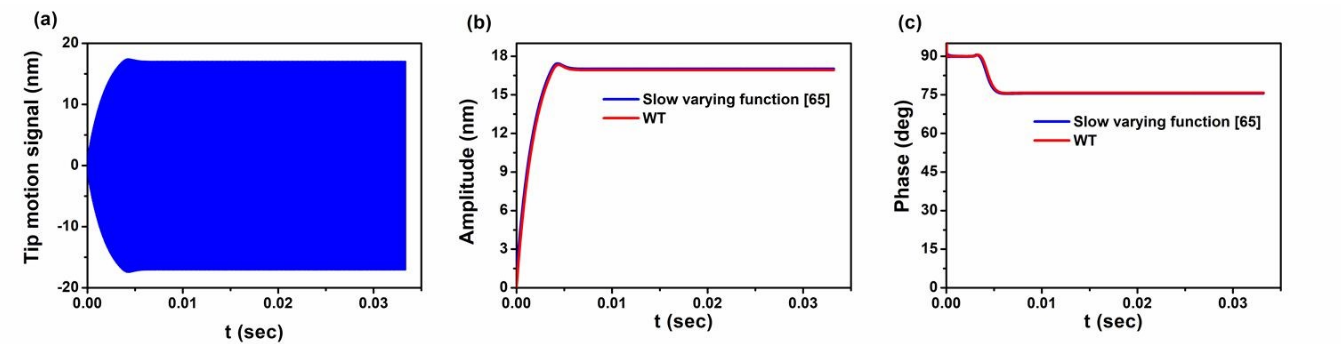

Figure 2. Comparison between simulations obtained using CWT and slow varying function [65] algorithms: a) tip motion signal of AFM in the repulsive regime in air environment, b) amplitude of the signal calculated by both CWT and slow varying function method [67] plotted against time, c) dynamics of the phase calculated by both CWT and slow varying function method [67] plotted against time [67]. In this simulation, the AFM parameters are chosen as: f_0

$= 300$ kHz, $Q = 300$, $k = 30$ N/m, $R_t = 5$ nm, $A_h = 10^{-19}$J, $E = 1$ GPa and $a_0 = 0.164$ nm, $A_0 = 20$ nm and $z_c = 16$ nm.

View Article Online
DOI: 10.1039/D0NA00531B

The possibility offered by the CWT method to convert a signal into a concise representation is illustrated in Figure 3. In this case, starting from a simulated signal (Figure 3.a) representing the original cantilever motion, CWT provides information about amplitude and phase into the magnitude (Figure 3.b) and XWT (Figure 3.c) phase maps, respectively. In turn, from the maps the separated signals of the first (Figures 3.d) and second (Figures 3.e) eigenfrequencies of the cantilever are extracted. In this simulation, the effect of the second eigenmode on the original signal is significant and distorts the signal when the cantilever is in contact with the sample, as highlighted in the magnitude scalogram (Figure 3.b). As it can be seen from Figure 3-a, during the contact with the sample, the cantilever experiences repulsive force that excite the second eigenmode of the cantilever. Finally, further calculations yield the wavelet coherence map (Figure 3.f), in which the direction of the arrows show the relative local phase of the cantilever signal in a unit circle, where the coherence is higher than 0.5. Analyzing XWT and local phase map, in this case, it can be inferred that the phase of the cantilever can be calculated at the first frequency with wavelet coherence of 1. It is therefore evident from this simple simulation that a distinct advantage offered by employing CWT on AFM signal is the extraction of information about harmonic effects in the time domain.

View Article Online
DOI: 10.1039/D0NA00531B

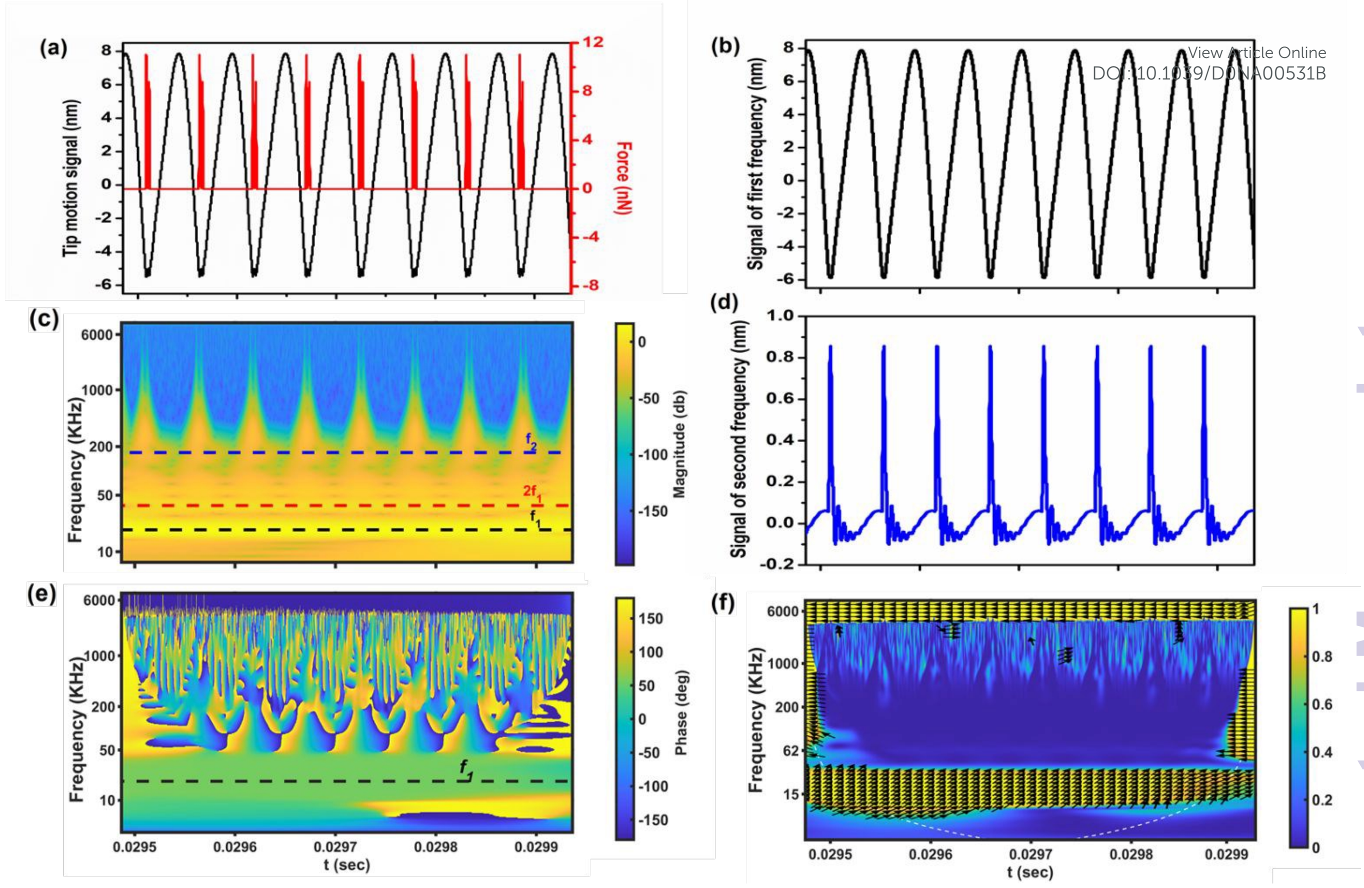

Figure 3. CWT time-frequency analysis of the tip motion signal. a) The original tip motion and interaction force between cantilever and sample, b) the magnitude scalogram of the signal represented in decibel, c) the XWT phase map of the simulated signal, d) signal of the first frequency of cantilever, e) signal of second frequency of cantilever, f) the coherence map. In the scalograms, the first and second eigenfrequencies and second harmonic frequency are represented by the horizontal dashed lines. The simulation parameters are: $f_{01} = 18.6$ kHz,$f_{02} = 170$ kHz, $Q_1 = 1.62$, $Q_2 = 4.526$, $k_1 = 0.22$ N/m, $k_1 = 12.23$ N/m, $R_t = 10$ nm, $E = 10$ GPa,and $a_0 = 0.164$ nm.

However, the main advantage offered by the CWT is the ability to produce data including information about the transient response of amplitude and phase in relation to the variation of materials properties and sample topography. To demonstrate it, we performed simulations of the probe-sample interaction both in an air and liquid environment (Figure 4) and applied the CWT method to the resulting signal. The changes across the sample surface have been simulated with varying probe-sample distance z_c (topography), Young modulus E (stiffness), viscosity η and Hamaker constant A_h (adhesion) at set time intervals.

DOI: 10.1039/D0NA00531B

The Figures 4.a to 4.c are the simulated results for liquid and 4.d to 4.f are simulated results for the air environment. For the simulation in a liquid environment, six different scenarios are considered by changing one of the parameters of the simulation at time. It starts with average cantilever-sample distance $z_c = 8$ nm, free amplitude $A_0 = 13.5$ nm and sample's Young modulus 1 GPa. After 0.005 seconds, the Young modulus is set to 100 MPa, leading to an increase in both amplitude and phase. In the case of the phase, decrease in the material's stiffness means that the repulsive interaction is reduced, giving rise to an increase of phase towards the attractive regime, as we know in attractive regime the phase is more than 90^o [67], [73], [74]. As well, the increase of amplitude is explained by the fact that the probe experiences less force from the sample. In a third step, the viscosity ($\eta = 100$ Pa.s) is included into the simulation. The responses to the change of viscosity are markedly different, with phase slightly increasing and amplitude decreasing. The increase of phase and decrease of amplitude is related to phase shift due to dissipation at repulsive regime. At $t = 0.015$ s the average distance of cantilever z_c is decreased, leading to decrease of both amplitude and phase, meaning that the cantilever experiences slightly more repulsive force. At t = 0.020 s the viscosity is decreased, which leads to decrease in phase and increase in amplitude. Finally, the Young modulus is increased leading to decrease in both phase and amplitude, meaning more force experienced by the cantilever, i.e. increase in repulsive force. From the results it can be summarized that increase of stiffness or decrease of average probe-sample distance leads to decrease of both amplitude and phase, while increase of viscosity leads to increase of phase and decrease of amplitude. In other words, the behavior of amplitude and phase with respect to change in viscosity is different while for the change in stiffness their behavior is the same. The responses of the amplitude of the second and third harmonics are depicted in Figure 4.c. Both harmonics have the same behavior corresponding to the changes of the simulation parameters while in some cases they have different behavior with respect to the amplitude of the main frequency, which is interesting to study. As it can be seen, decreasing the Young modulus, in contrast to main frequency amplitude behavior, leads to decrease of harmonics which can be expected given that the interaction force is decreased. Increasing the viscosity also slightly reduces

View Article Online
DOI: 10.1039/D0NA00531B

the magnitude of harmonics, showing in this case the same behavior for the harmonics and main amplitude. Reducing the average distance leads to an increase of harmonics while the main amplitude is decreased. Then, reduction of viscosity not only increases the main amplitude but also magnifies the harmonics. Finally, increasing the Young modulus increases the magnitude of harmonics while decrease the main amplitude. To analyze the behavior of harmonics of the cantilever in liquid environment due to the changes of parameters, it can be summarized that increasing Young-modulus and decreasing average distance - which reduces the main amplitude due to experiencing higher repulsive force - increases the magnitude and effect of harmonics on the main signal. The interesting point of this result is the impact of increase (decrease) of viscosity or in other words dissipation, on the magnitude of harmonics. With respect to changes in dissipation, the harmonics of the cantilever signal have the same behavior as the main amplitude and increasing (decreasing) the viscosity leads to the decrease (increase) of the amplitude of the second and third harmonics of cantilever. The effect of the parameter's changes on higher harmonics and second frequency of cantilever is shown in supplementary information.

To study the behavior of the main amplitude, phase and second/third harmonics of cantilever in air environment, eight scenarios are considered. It is worthy to mention that in air environment, due to the increase of quality factor, the effect on harmonics and eigenfrequencies are very low in comparison with the case of liquid medium. The simulation starts with $z_c = 8$ nm , free amplitude $A_0 = 10$ nm, Hamaker constant 10^{-20}J and Young modulus of the sample 1 GPa.

After 0.005 seconds the Young modulus of sample is decreased, resulting in increase of main amplitude and phase and decrease of second and third harmonics. This is due to the reduction of repulsive force and transition from repulsive to attractive regime. Increase of sample's viscosity to 100 Pa.s yields slight decrease of phase (from 126^o to 125.7^o) and main amplitude. In contrast to the simulation in liquid environment, the behavior of amplitude and phase is the same. This phenomenon has been explained [68], [69] as originating from the difference of phase contrast in air and liquid

View Article Online
DOI: 10.1039/D0NA00531B

environment. At $t = 0.015$ s an increase of Young modulus from 100 MPa to 1 GPa leads to the increase in amplitude and decrease in phase. Increase of main amplitude - as it is obvious from phase value - is due to the fact that being the interaction in attractive regime an increasing in stiffness leads to decrease of attractive force, leading to decrease of phase value below 90^o and increase in main amplitude. Increasing the Hamaker constant tenfold, meaning higher attractive force, leads to slight increase in phase and decrease of main amplitude. At 0.025 s decrease in average distance leads to decrease in amplitude and increase in phase meaning that the interaction approaches maximum attractive force. Decreasing the Hamaker constant leads to increase in amplitude and decrease in phase due to the lower value of attractive force. Finally, decrease in viscosity, moving the interaction into repulsive regime, increases the amplitude and decreases the phase. In this case the behavior of phase and amplitude is different same as liquid environment due to the presence of repulsive regime. The harmonics increase slightly, which means that reduction of dissipation makes the transition from attractive to repulsive regime causes different behavior between phase and amplitude than attractive regime [68], [69]. The scalograms of the simulation is given in Supplementary information.

View Article Online
DOI: 10.1039/D0NA00531B

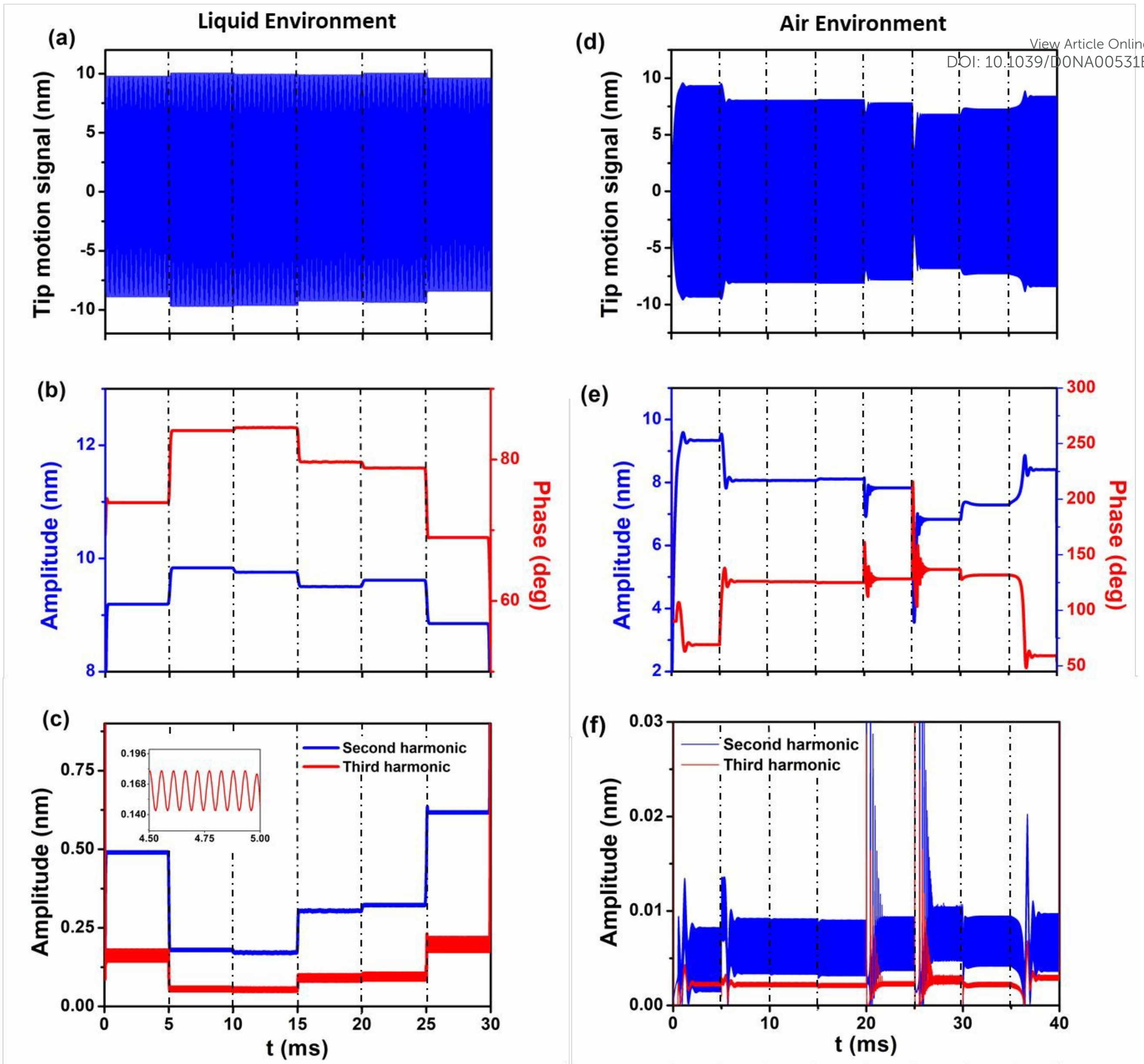

E [Gpa]	1	0.1	0.1	0.1	0.1	0.5
η [PA.s]	0	0	100	100	10	10
Z_c[nm]	8	8	8	7	7	7

E [Gpa]	1	0.1	0.1	1	1	1	1	1
η [PA.s]	0	0	100	100	100	100	100	10
Z_c[nm]	8	8	8	8	8	7	7	7
A_k[10^{-20}J]	1	1	1	1	10	10	1	1

Figure 4. CWT model simulation: comparison between liquid (a,b,c) and air (d,e,f) environments: a) original signal of tip motion in liquid, b) amplitude and phase versus time response obtained from CWT analysis in liquid environment, c) amplitude response of second and third harmonics obtained from CWT analysis, d) original signal of tip motion in air environment, e) amplitude and phase versus time response from CWT analysis in air environment in both attractive and repulsive regimes, f) amplitude response of second and third harmonics obtained from CWT analysis.

View Article Online
DOI: 10.1039/D0NA00531B

After comprehensive analysis of the dynamic response of the cantilever calculated using the continuous wavelet transform on simulated data, we applied the proposed method to the time domain data from actual measurements and compare the results to the data elaborated by the embedded LIA in the AFM system. Amplitude and phase images are generated by CWT as whole signals including transient responses, but for the sake of comparison with the images captured by the AFM system they are reduced to pixel AFM resolution by averaging them over the time interval of each pixel. Performing this operation on one set of data acquired on the calibration sample (sample 1) produces results showing a very good agreement between the two sets of images (Figure 5), not only for the amplitude but for the phase signal as well.

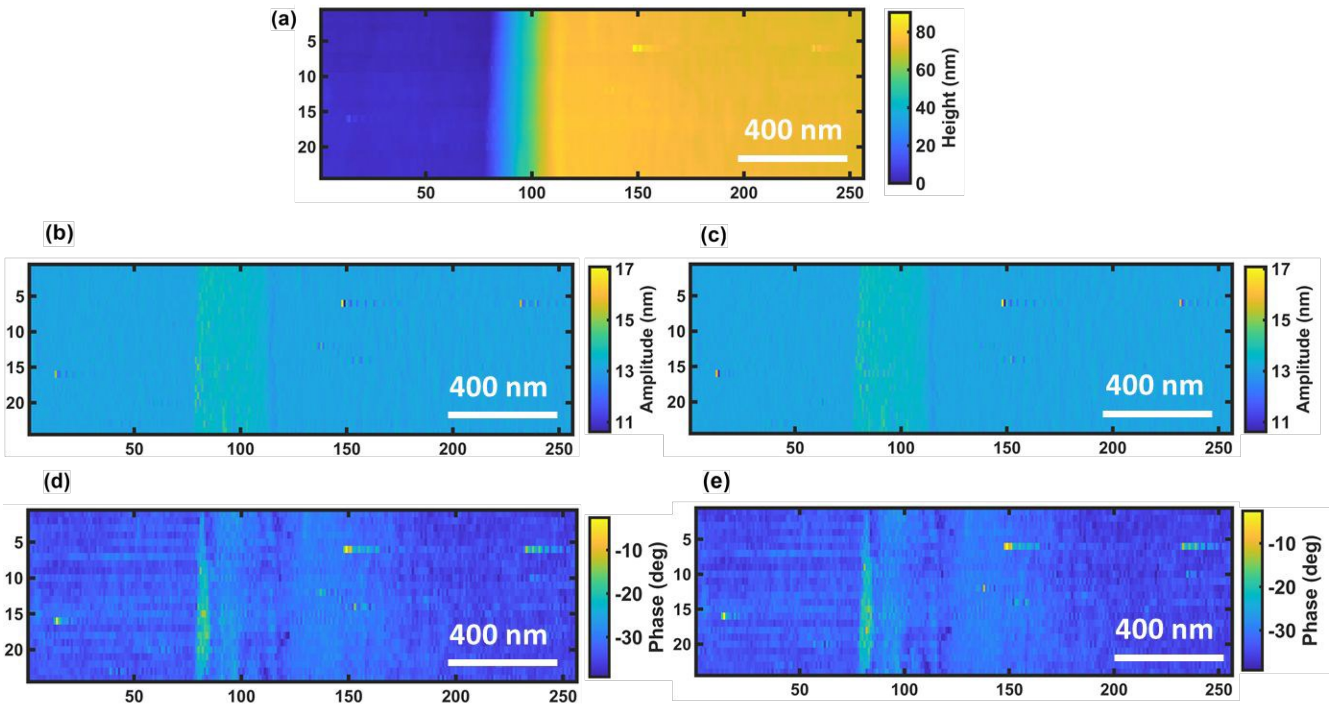

Figure 5. Comparison between standard LIA images (commercial AFM-tapping instrument) and reconstructed ones by CWT for sample 1. a) The topography of the sample, b) the amplitude image of standard LIA, c) the reconstructed amplitude image calculated by CWT, d) the phase image of standard LIA, e) the reconstructed phase image calculated by XWT.

Non-averaged images obtained by the CWT carry a greater deal of information than the ones provided by the AFM system, mainly due to the fact that the CWT provides a time-frequency analysis of a

View Article Online
DOI: 10.1039/D0NA00531B

signal. Therefore, the CWT and its coherence are capable of calculating the amplitude and phase of the signal at all the available datapoints and the only limitation would be the computational cost of applying this signal processing method. Comparison of images obtained by the standard averaging procedure and whole points captured by CWT (Figure 6b-6e), especially between line profile of the same line (Figure 6f-6i), not only shows the capability of CWT to provide standard images based on averaging procedure, but also shows significant enhancement of the quality and resolution of the temporal CWT images, since the operation of averaging at each pixels yields to information loss in the image with respect to the whole response. Such loss of information becomes critical in case fast dynamic response information from the sample needs to be analyzed. Moreover, computation of material properties starting from data extracted from averaged images might be affected and possibly lead to significant error due to the sensitivity of computation at the nanoscale. Note that in this figure we use the same color bar for images based on the maximum and minimum values of averaged images. The same images but considering max and min values of temporal CWT images are shown in Supplementary information (FigS4) which represents CWT's potential in illustrating the details of an image compared to averaged images. Further details are provided in the supplementary information section (Figures S5 and S6).

View Article Online
DOI: 10.1039/D0NA00531B

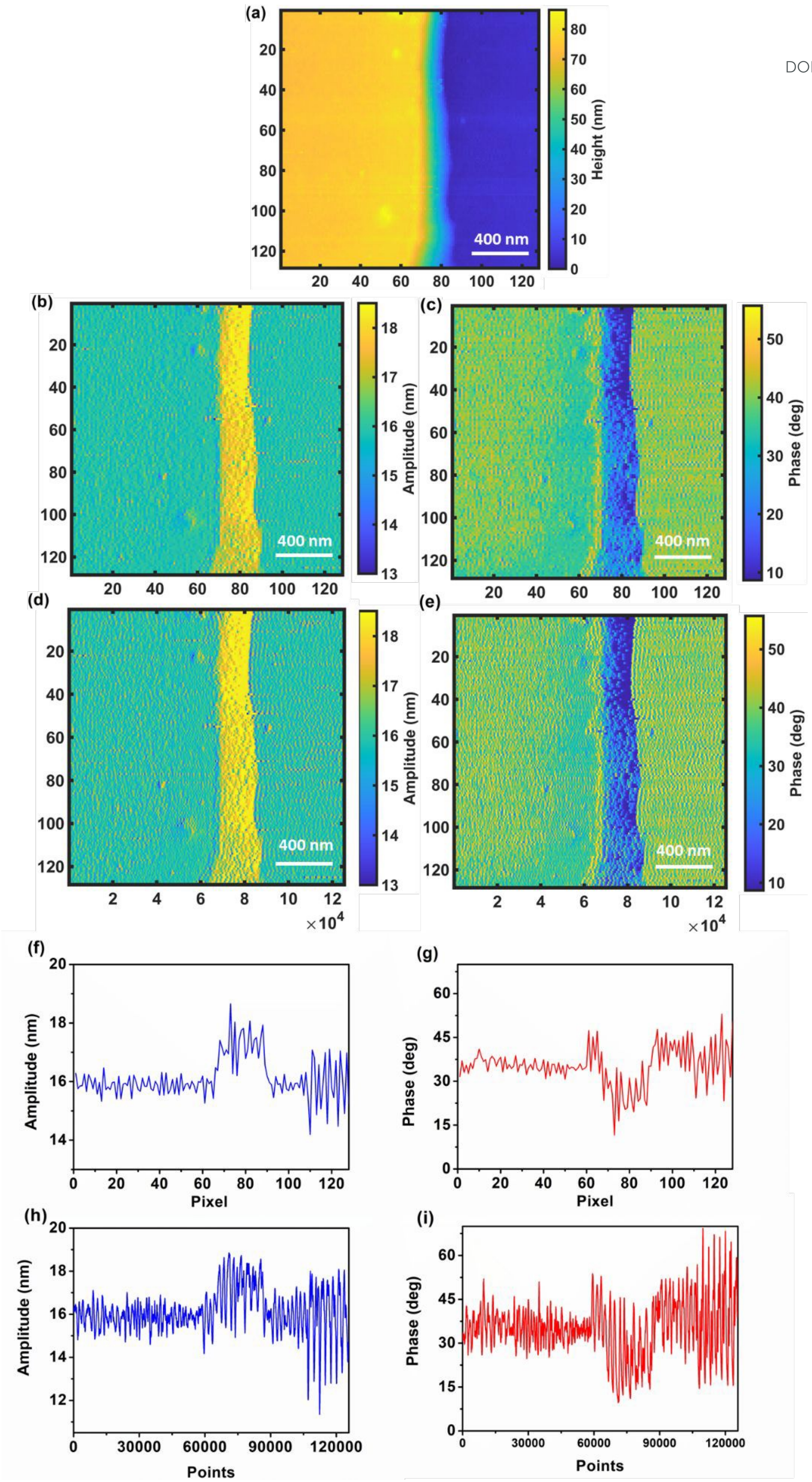

Figure 6. Comparison between standard averaged image (256 pixel scale – b ,c ,f, g) and CWT image (whole 120000 pixel scale –d,e,h,i) for sample 1.(a) topography image of the sample, (b,d) amplitude images and (c,e) phase images. The line scans (f-i) are for line 105 of images.

View Article Online
DOI: 10.1039/D0NA00531B

Figures 7a and 7b show the real time cantilever signal of line 21 of Y axis in the scanned image of Figure 6 directly obtained by photodetector.

Figures 7c-7f show the information extracted by CWT from the photodetector signal of Figures 7a and 7b. Both trace and retrace of the signal are analyzed, obtaining the magnitude scalogram and XWT phase map. The associated tip motion signals and the transient response of amplitude and phase are given in figures 7e to 7j. It is noteworthy highlighting that with this procedure all the dynamics of the signals of cantilever are captured and recorded in scalograms and can be recovered at any time. On the contrary, with standard AFM data acquisition and processing, the transient response is lost due to averaging and use of stationary spectral analysis. From the behavior of amplitude and phase with respect to the time it is completely obvious that the cantilever experiences the height changes of the calibration sample. Comparison between line 21 of the amplitude and phase images with the real time response of amplitude and phase in Figure 7g and 7i shows the effect of the height variation and details of cantilever motion in the response of amplitude and phase which can be easily seen in the results from CWT analysis. It is important to mention that the trace and retrace amplitude and phase signals are direction-dependent, which is easily understood by considering the case of amplitude: the probe passing over an ascending (descending) step will experience a decrease (increase) in amplitude before the feedback adjusts the probe-sample distance. For this reason, at the same step, the amplitude signal is increased in the trace while it is decreased in the retrace direction. For the phase signal the explanation is the same.

View Article Online
DOI: 10.1039/D0NA00531B

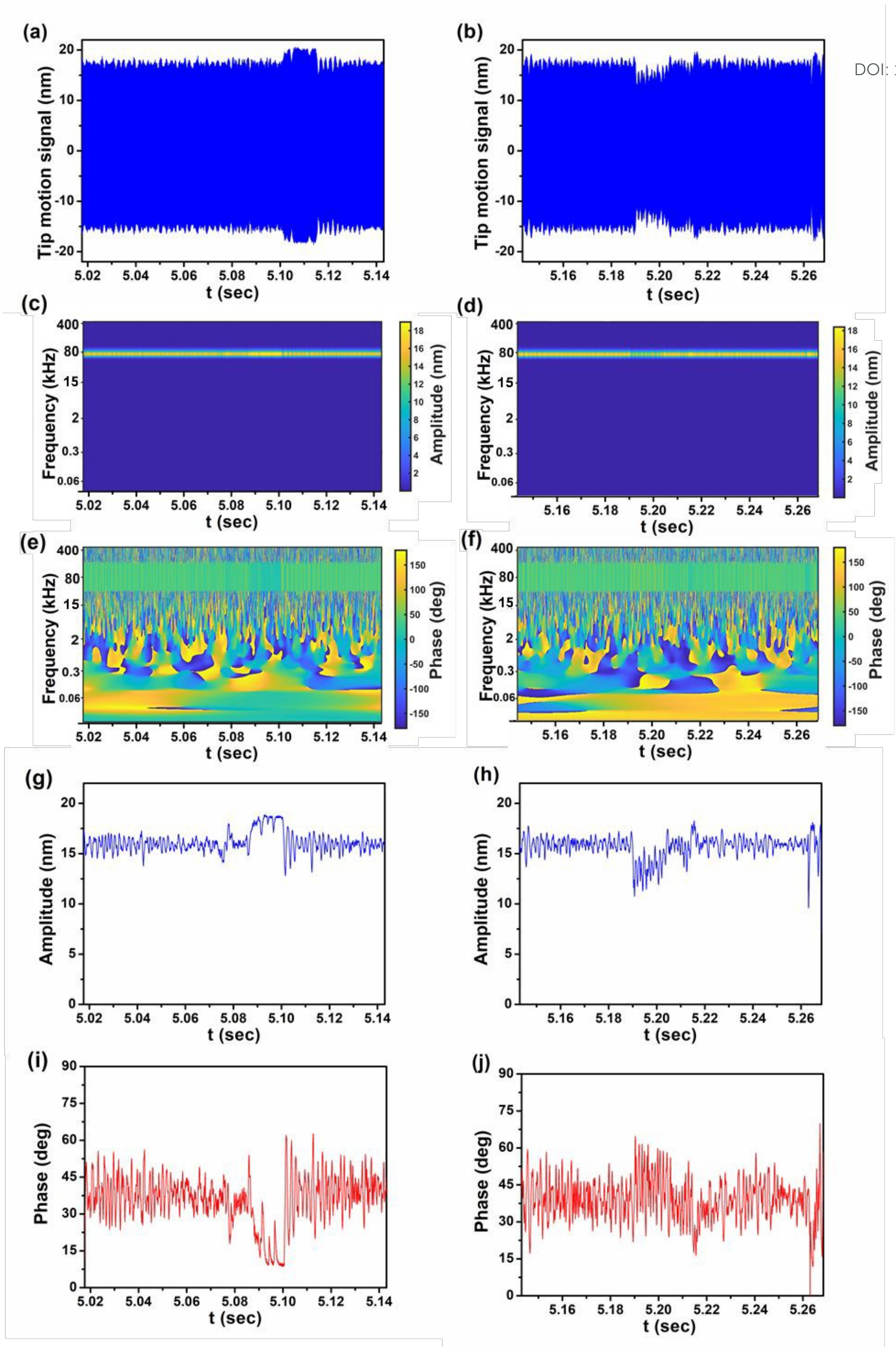

Figure 7. CWT analysis of the experimental signal obtained from imaging sample 1. a) and b) original cantilever tip motion signal of trace and retrace, respectively, c) and d) magnitude scalograms of the trace and retrace signals, respectively, e) and f) XWT phase maps of the trace and retrace signals, respectively, g) and h) real time amplitude response of trace and retrace signals, i) and j) real time phase response of trace and retrace signals, respectively.

View Article Online
DOI: 10.1039/D0NA00531B

In order to show the CWT's capability to provide nonlinear and multifrequency information of cantilever sample interaction, we plot the amplitude maps of non-integer harmonics. Due to the CWT's capability in transforming the signal into daughter wavelets with different scales, where each contains the information of a range of frequencies available in the signal, it is possible to plot the images of non-integer harmonics and side band simultaneously in the wide range of frequencies around excited frequency of the cantilever. The non-integer harmonics are associated with a frequency of transient beats occurred on the cantilever and can provide information about the interaction force and transient instability of the cantilever interacted with sample surface [75]–[79]. The proposed CWT methodology in detecting simultaneously non-integer harmonics, harmonics and eigenfrequencies can provide an opportunity to extract more physical and chemical information from images and acquired data of interaction. Figure 8 exhibits the non-integer harmonic amplitude images of sample 1 (calibration sample) between 0.7 to 1.5 times of main frequency. As it can be seen, the amplitude of non-integer harmonics is different and as the frequency is closer to the main frequency the amplitude increases. For this purpose, the images are plotted in different color scales to better show the data that are saved in different non-integer harmonics. The comparison between non-integer harmonics images shows that the resolution of images in the non-integer harmonics that are higher than main frequency is better than those with values lower than main frequency. Moreover, as the non-integer harmonic is closer to the main frequency, the resolution is closer to the image of main frequency. Furthermore, the range of amplitudes in each graph is also different for different non-integer harmonics. Non-integer harmonic of $0.7f$ exhibits lowest amplitude and lowest range of amplitude while non-integer harmonic of $1.1f$ has the closest amplitude and amplitude range to the main frequency. Comparison between $1.3f$ and $0.7f$ shows higher amplitude for $1.3f$ which depicts for the case of same frequency difference respect to main frequency, the amplitude of non-integer harmonics with frequency higher than main frequency is higher than those with lower frequency. From the acquired data, it can be summarized that the distribution and amplitude of non-integer harmonics are not symmetric around the main frequency of the signal which can be related to the nonlinear nature of interaction force. So, CWT can be considered as a versatile tool to study the interplay between materials properties and nonlinearity and transient of cantilever to explore more information about the stability of imaging and extract physical, chemical, and mechanical information from the samples.

View Article Online
DOI: 10.1039/D0NA00531B

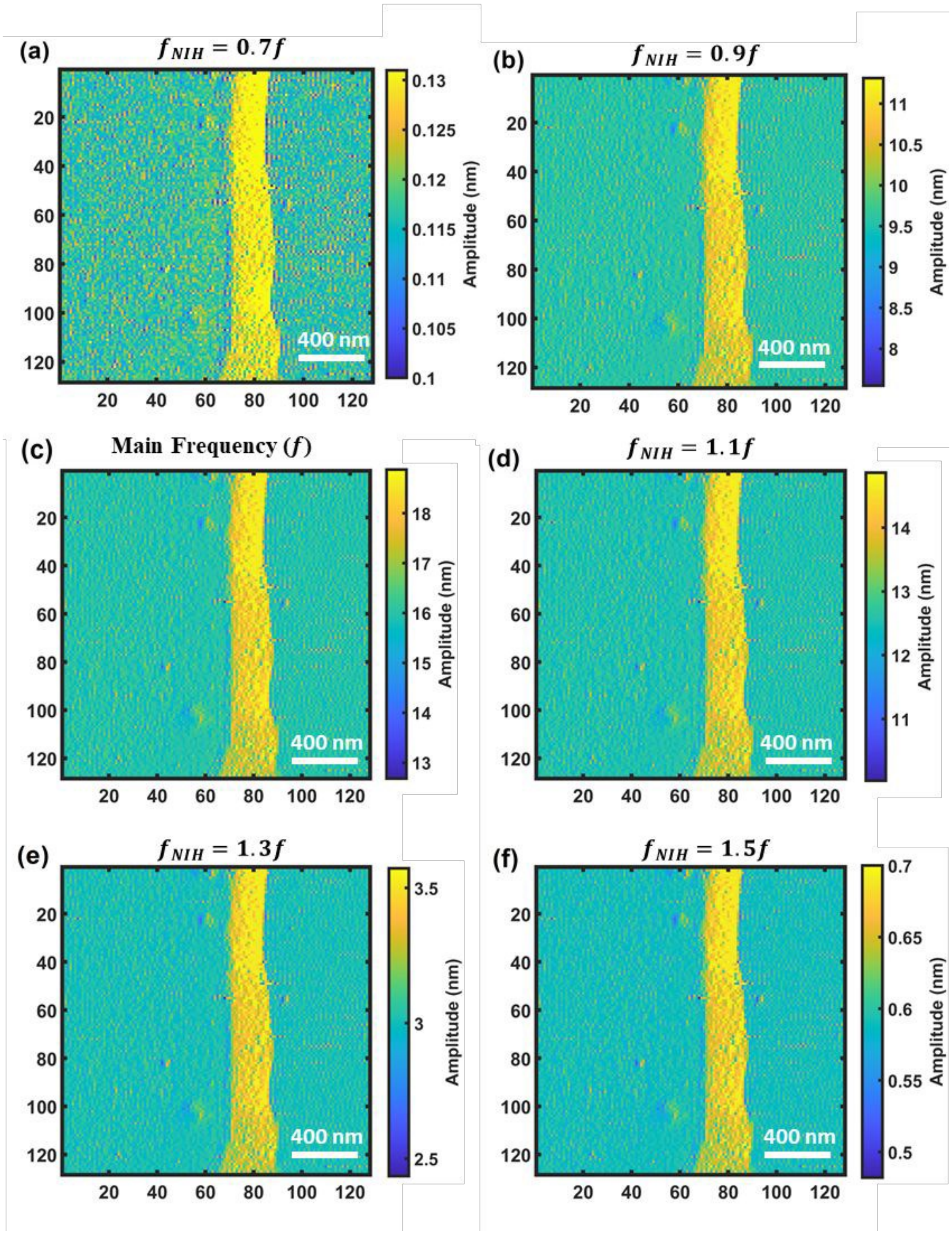

Figure 8. Non-integer harmonic images of sample 1. a) Amplitude image at $0.7f$ (51 kHz), b) amplitude image at $0.9f$ (65.6 kHz), c) amplitude image at main frequency ($f = 72.96$ kHz) d) amplitude image at $1.1f$ (80.2 kHz), e) amplitude image at $1.3f$ (94.8 kHz), f) amplitude image at $1.5f$ (109.4 kHz).

View Article Online
DOI: 10.1039/D0NA00531B

Finally, in order to show the performance of our method to detect the transient responses in presence of continuous topography variations, a measurement and analysis on a typical AFM probe qualification sample, sample 2, have been performed. Figure 9f to 9i show the averaged and real time amplitude and phase response of cantilever of line 14 of the images of Figure 9b to 9e. As it can be seen here the variation in real time response of amplitude and phase can be detected precisely, while in the averaged amplitude and phase the data from the signal dynamics are lost. This is strongly proving the capability of the proposed technique to detect the transient response of the cantilever. As for the calibration sample measurement and analysis, images and line profile comparison clearly show loss of information during averaging.

View Article Online
DOI: 10.1039/D0NA00531B

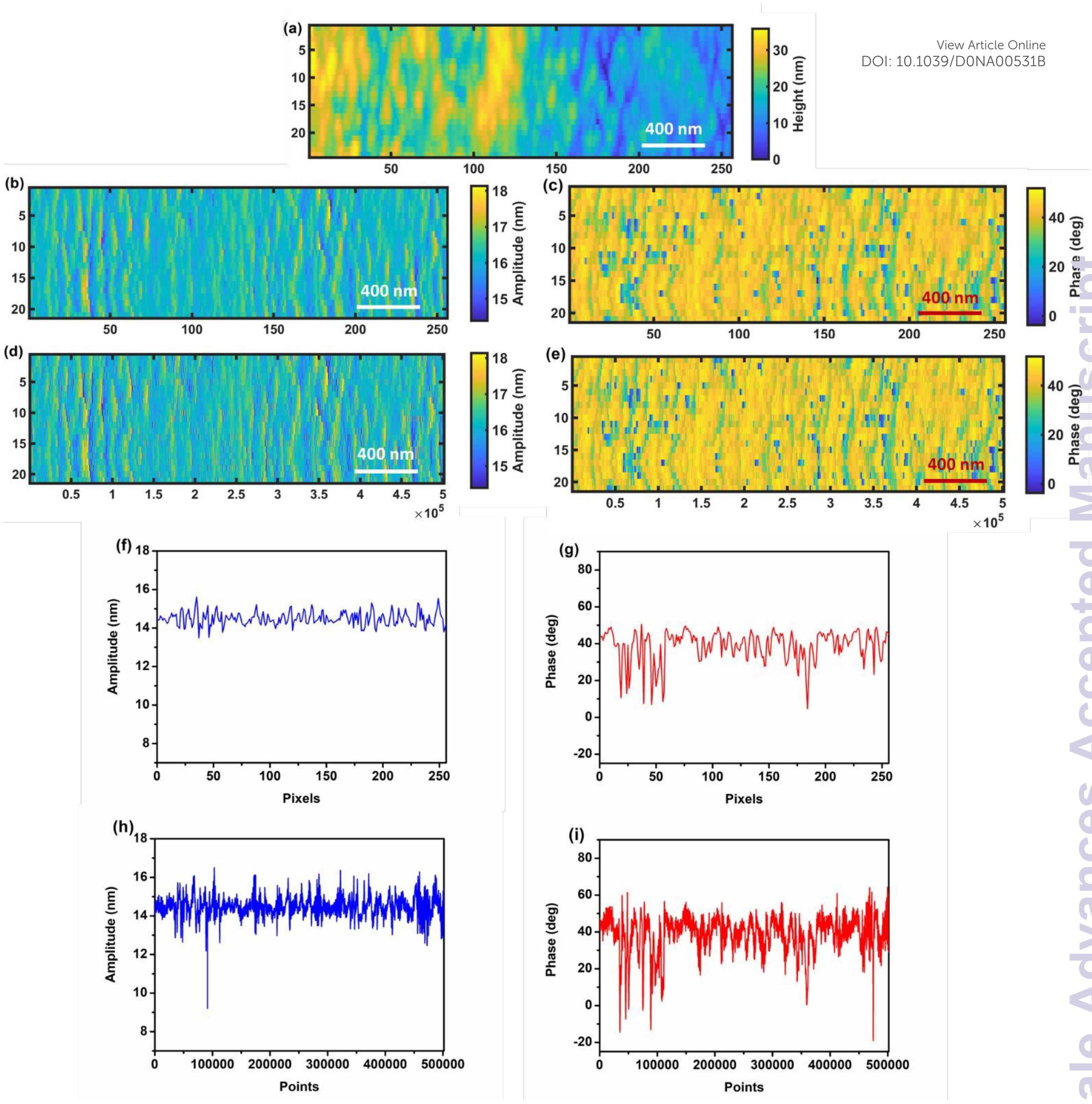

Figure 9. Comparison between standard averaged image (average x pixel scale; and b,c,f,g) CWT analysis (whole x pixel scale; d,e,h,i) for sample 2. a) topography image, b) averaged amplitude image, c) averaged phase image, d) whole amplitude image, e) whole phase image of qualification sample obtained by XWT. f) and g) averaged amplitude and phase signals and h) and i) real time amplitude and phase signals of line 14 of qualification sample captured by CWT.

In order to show the capability of the CWT to detect the transient response of the cantilever we plot the histogram of the amplitudes detected by CWT and compare the data with the detected amplitudes of standard LIA used in commercial AFMs (Figure 10). As it can be seen, the distribution of

View Article Online
DOI: 10.1039/D0NA00531B

amplitudes in CWT histogram is significantly wider than LIA which means that when using CWT all of the transient and changes that cantilever experienced can be detected while in LIA due to its detection mechanism which is based on steady state regime of the signal and also averaging the data, the transient and fast changes of the signal is lost. The non-integer harmonics detail of sample 2 are given in Supplementary Information.

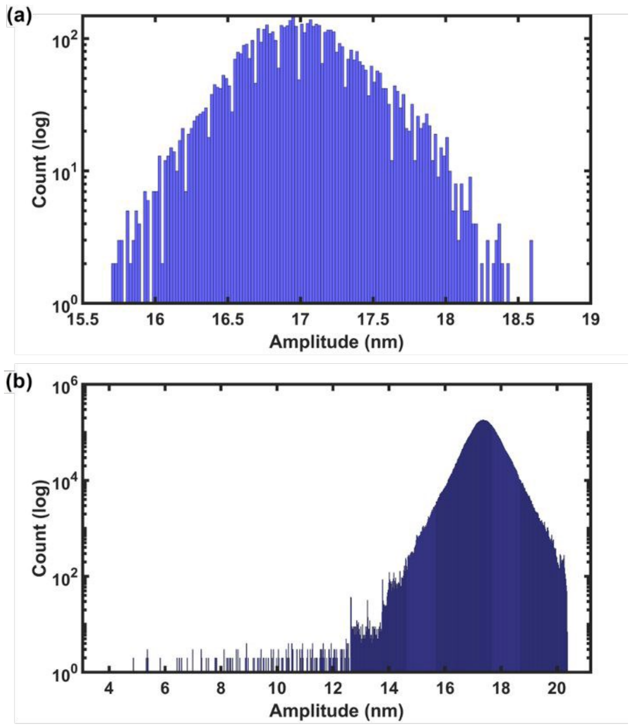

Figure 10. Histogram of amplitudes of the signal detected by a) LIA and b) CWT during imaging.

5. Conclusion

For the first time the CWT method was used to extract the steady state and transient responses of both the amplitude and phase signals for an AFM cantilever operated in amplitude modulation AFM, providing AFM images informative of the whole dynamics of the tip/surface system.

By use of simulations, we proved the capability of the method to produce data including information about the transient response of amplitude and phase in relation to the variation of materials properties and sample topography. The technique was successfully used to reconstruct amplitude and phase images of standard samples, starting from time domain data from actual measurements. The results match and surpass in details richness the images generated by standard LIA analysis.

Finally, this novel concept, by integration within the feedback system of the AFM setup, can be used to control probe movement, opening the path for high-speed transient force microscopy. Substitution of LIA feedback – with its inherent bandwidth limitation – with CWT method would in first place improve measurements speed, and secondly reduce information loss, giving access to a wealth information about transient response, leading to the possibility to analyze in detail material properties in dynamic AFM.

View Article Online
DOI: 10.1039/D0NA00531B

Acknowledgements

The authors acknowledge funding from the European Union's INTERREG VA Programme, managed by the Special EU Programmes Body (SEUPB). Furthermore, we would like to acknowledge the funding support from Invest N. Ireland (RD0714186) for AM.

* AF Payam and P Biglarbeigi have equal contribution

References

[1] C. A. Amo, A. P. Perrino, A. F. Payam, and R. Garcia, "Mapping Elastic Properties of Heterogeneous Materials in Liquid with Angstrom-Scale Resolution," *ACS Nano*, vol. 11, no. 9, pp. 8650–8659, 2017.

[2] Y. M. Efremov, A. X. Cartagena-Rivera, A. I. M. Athamneh, D. M. Suter, and A. Raman, "Mapping heterogeneity of cellular mechanics by multi-harmonic atomic force microscopy," *Nat. Protoc.*, vol. 13, no. 10, pp. 2200–2216, 2018.

[3] Y. F. Dufrêne *et al.*, "Imaging modes of atomic force microscopy for application in molecular and cell biology," *Nat. Nanotechnol.*, vol. 12, no. 4, pp. 295–307, 2017.

[4] B. Huang, Z. Li, and J. Li, "An artificial intelligence atomic force microscope enabled by machine learning," *Nanoscale*, vol. 10, no. 45, pp. 21320–21326, 2018.

[5] G. Rosso, I. Liashkovich, and V. Shahin, "In Situ Investigation of Interrelationships Between Morphology and Biomechanics of Endothelial and Glial Cells and their Nuclei," *Adv. Sci.*, vol. 6, no. 1, 2019.

[6] L. Mennel, J. Symonowicz, S. Wachter, D. K. Polyushkin, A. J. Molina-Mendoza, and T. Mueller, "Ultrafast machine vision with 2D material neural network image sensors," *Nature*, vol. 579, no. 7797, pp. 62–66, 2020.

[7] S. C. Warren *et al.*, "Identifying champion nanostructures for solar water-splitting," *Nat. Mater.*, vol. 12, no. 9, pp. 842–849, 2013.

[8] M. R. Uhlig, D. Martin-Jimenez, and R. Garcia, "Atomic-scale mapping of hydrophobic layers on graphene and few-layer MoS2 and WSe2 in water," *Nat. Commun.*, vol. 10, no. 1,

pp. 1–7, 2019.

[9] E. J. Miller, W. Trewby, A. Farokh Payam, L. Piantanida, C. Cafolla, and K. Voïtchovsky, "Sub-nanometer Resolution Imaging with Amplitude-modulation Atomic Force Microscopy in Liquid," *J. Vis. Exp.*, no. 118, pp. 1–10, 2016.

[10] A. Belianinov, S. V. Kalinin, and S. Jesse, "Complete information acquisition in dynamic force microscopy," *Nat. Commun.*, vol. 6, no. May 2014, pp. 1–7, 2015.

[11] N. Borodinov, S. Neumayer, S. V. Kalinin, O. S. Ovchinnikova, R. K. Vasudevan, and S. Jesse, "Deep neural networks for understanding noisy data applied to physical property extraction in scanning probe microscopy," *npj Comput. Mater.*, vol. 5, no. 1, pp. 1–8, 2019.

[12] K. Voitchovsky, J. J. Kuna, S. A. Contera, E. Tosatti, and F. Stellacci, "Direct mapping of the solid-liquid adhesion energy with subnanometre resolution," *Nat. Nanotechnol.*, vol. 5, no. 6, pp. 401–405, 2010.

[13] D. A. W. M. V. Hansma *et al.*, "Atomic force microscopy using small cantilevers," in *Photonics West '97, 1997, San Jose, CA, United States*, 1997.

[14] P. K. Hansma, G. Schitter, G. E. Fantner, and C. Prater, "High-Speed Atomic Force Microscopy," *Science (80-.).*, vol. 314, no. 5799, pp. 601–602, 2006.

[15] J. D. Adams, A. Nievergelt, B. W. Erickson, C. Yang, M. Dukic, and G. E. Fantner, "High-speed imaging upgrade for a standard sample scanning atomic force microscope using small cantilevers," *Rev. Sci. Instrum.*, vol. 85, no. 9, 2014.

[16] D. Knebel, M. Amrein, K. Voigt, and R. Reichelt, "A fast and versatile scan unit for scanning probe microscopy," *Scanning*, vol. 19, no. 4, pp. 264–268, 1997.

[17] N. Kodera, M. Sakashita, and T. Ando, "Dynamic proportional-integral-differential controller for high-speed atomic force microscopy," *Rev. Sci. Instrum.*, vol. 77, no. 8, p. 083704, 2006.

[18] T. Ando, N. Kodera, Y. Naito, T. Kinoshita, K. Furuta, and Y. Y. Toyoshima, "A High-speed Atomic Force Microscope for Studying Biological Macromolecules in Action," *Proc. Natl. Acad. Sci. U. S. A.*, vol. 98, pp. 12468–12472, 2003.

[19] Y. Wu, J. Shi, C. Su, and Q. Zou, "A control approach to cross-coupling compensation of piezotube scanners in tapping-mode atomic force microscope imaging," *Rev. Sci. Instrum.*, vol. 80, no. 4, 2009.

[20] A. S. G Schitter, F Allgöwer, "A new control strategy for high-speed atomic force microscopy," *Nanotechnology*, vol. 15, no. 1, pp. 108–114, 2004.

[21] G. Schitter and A. Stemmer, "Identification and open-loop tracking control of a piezoelectric tube scanner for high-speed scanning-probe microscopy," *IEEE Trans. Control Syst. Technol.*, vol. 12, no. 3, pp. 449–454, 2004.

[22] A. D. L. Humphris, M. J. Miles, and J. K. Hobbs, "A mechanical microscope: High-speed atomic force microscopy," *Appl. Phys. Lett.*, vol. 86, no. 3, pp. 1–3, 2005.

[23] M. A. H. and M. J. M. L M Picco, L Bozec, A Ulcinas, D J Engledew, M Antognozzi, "Breaking the speed limit with atomic force microscopy," *Nanotechnology*, vol. 18, p. 0044030, 2007.

[24] G. Schitter, "Advanced mechanical design and control methods for atomic force microscopy in real-time," *Proc. Am. Control Conf.*, pp. 3503–3508, 2007.

View Article Online
DOI: 10.1039/D0NA00531B

[25] B. J. Kenton and K. K. Leang, “Design and control of a three-axis serial-kinematic high-bandwidth nanopositioner,” *IEEE/ASME Trans. Mechatronics*, vol. 17, no. 2, pp. 356–369, 2012.

[26] B. J. Kenton, “Design, Characterization, and Control of a High-Bandwidth Serial-Kinematic Nanopositioning Stage for Scanning Probe Microscopy Applications,” University of Nevada, 2010.

[27] B. J. Kenton and K. K. Leang, “Flexure design using metal matrix composite materials: Nanopositioning example,” *Proc. - IEEE Int. Conf. Robot. Autom.*, pp. 4768–4773, 2012.

[28] T. Ando, “High-speed atomic force microscopy coming of age,” *Nanotechnology*, vol. 23, no. 6, 2012.

[29] M. G. Ruppert, D. M. Harcombe, M. R. P. Ragazzon, S. O. Reza Moheimani, and A. J. Fleming, “A review of demodulation techniques for amplitude-modulation atomic force microscopy,” *Beilstein J. Nanotechnol.*, vol. 8, no. 1, pp. 1407–1426, 2017.

[30] D. M. Harcombe, M. G. Ruppert, and A. J. Fleming, “A review of demodulation techniques for multifrequency atomic force microscopy,” *Beilstein J. Nanotechnol.*, vol. 11, pp. 76–91, 2020.

[31] M. Ayat, M. A. Karami, S. Mirzakuchaki, and A. Beheshti-Shirazi, “Design of Multiple Modulated Frequency Lock-In Amplifier for Tapping-Mode Atomic Force Microscopy Systems,” *IEEE Trans. Instrum. Meas.*, vol. 65, no. 10, pp. 2284–2292, 2016.

[32] T. Uchihashi, T. Ando, and H. Yamashita, “Fast phase imaging in liquids using a rapid scan atomic force microscope,” *Appl. Phys. Lett.*, vol. 89, no. 21, 2006.

[33] J. Kokavecz, Z. Tóth, Z. L. Horváth, P. Heszler, and Á. Mechler, “Novel amplitude and frequency demodulation algorithm for a virtual dynamic atomic force microscope,” *Nanotechnology*, vol. 17, no. 7, 2006.

[34] D. Y. Abramovitch, *Low latency demodulation for Atomic Force Microscopes, part II: Efficient calculation of magnitude and phase*, vol. 44, no. 1 PART 1. IFAC, 2011.

[35] D. Y. Abramovitch, “Efficient Real-Time Integration,” pp. 2252–2257, 2011.

[36] D. M. Harcombe, M. G. Ruppert, M. R. P. Ragazzon, and A. J. Fleming, “Lyapunov estimation for high-speed demodulation in multifrequency atomic force microscopy,” *Beilstein J. Nanotechnol.*, vol. 9, no. 1, pp. 490–498, 2018.

[37] M. G. Ruppert, K. S. Karvinen, S. L. Wiggins, and S. O. R. Moheimani, “A Kalman Filter for Amplitude Estimation in High-Speed Dynamic Mode Atomic Force Microscopy,” *IEEE Trans. Control Syst. Technol.*, vol. 24, no. 1, pp. 276–284, 2016.

[38] H. Söngen, R. Bechstein, and A. Kühnle, “Quantitative atomic force microscopy,” *J. Phys. Condens. Matter*, vol. 29, no. 27, 2017.

[39] T. Wagner, “Steady-state and transient behavior in dynamic atomic force microscopy,” *J. Appl. Phys.*, vol. 125, no. 4, 2019.

[40] A. F. Payam, D. Martin-Jimenez, and R. Garcia, “Force reconstruction from tapping mode force microscopy experiments,” *Nanotechnology*, vol. 26, no. 18, pp. 1–12, 2015.

[41] Z. Wang *et al.*, “Time-frequency analysis of the tip motion in liquids using the wavelet transform in dynamic atomic force microscopy,” *Nanotechnology*, vol. 29, no. 38, 2018.

[42] Z. Wang *et al.*, “Wavelet analysis of higher harmonics in tapping mode atomic force

microscopy," *Micron*, vol. 118, no. November 2018, pp. 58–64, 2019.

[43] F. Banfi and G. Ferrini, "Wavelet cross-correlation and phase analysis of a free cantilever subjected to band excitation," *Beilstein J. Nanotechnol.*, vol. 3, no. 1, pp. 294–300, 2012.

[44] G. Malegori and G. Ferrini, "Wavelet transforms to probe long-and short-range forces by thermally excited dynamic force spectroscopy," *Nanotechnology*, vol. 22, no. 19, 2011.

[45] Mallat Stephane, *Signal Processing A Wavelet Tour of The Sparse Way*. 1999.

[46] M. Carmichael, R. Vidu, A. Maksumov, A. Palazoglu, and P. Stroeve, "Using wavelets to analyze AFM images of thin films: Surface micelles and supported lipid bilayers," *Langmuir*, vol. 20, no. 26, pp. 11557–11568, 2004.

[47] V. Pukhova, F. Banfi, and G. Ferrini, "Transient eigenmodes analysis of single-impact cantilever dynamics combining Fourier and wavelet transforms," *Nanotechnology*, vol. 26, no. 17, pp. 1–10, 2015.

[48] E. A. López-Guerra, F. Banfi, S. D. Solares, and G. Ferrini, "Theory of Single-Impact Atomic Force Spectroscopy in liquids with material contrast," *Sci. Rep.*, vol. 8, no. 1, pp. 1–16, 2018.

[49] V. Pukhova and G. Ferrini, "Multi-frequency data analysis in AFM by wavelet transform," *IOP Conf. Ser. Mater. Sci. Eng.*, vol. 256, no. 1, 2017.

[50] V. Pukhova, F. Banfi, and G. Ferrini, "Energy dissipation in multifrequency atomic force microscopy," *Beilstein J. Nanotechnol.*, vol. 5, no. 1, pp. 494–500, 2014.

[51] V. Pukhova, F. Banfi, and G. Ferrini, "Complex force dynamics in atomic force microscopy resolved by wavelet transforms," *Nanotechnology*, vol. 24, no. 50, 2013.

[52] B. Laperrousaz *et al.*, "Revealing stiffening and brittling of chronic myelogenous leukemia hematopoietic primary cells through their temporal response to shear stress," *Phys. Biol.*, vol. 13, no. 3, 2016.

[53] C. Martinez-Torres, A. Arneodo, L. Streppa, P. Argoul, and F. Argoul, "Passive microrheology of soft materials with atomic force microscopy: A wavelet-based spectral analysis," *Appl. Phys. Lett.*, vol. 108, no. 3, 2016.

[54] H. Xie, Y. Wen, X. Shen, H. Zhang, and L. Sun, "High-Speed AFM Imaging of Nanopositioning Stages Using H∞ and Iterative Learning Control," *IEEE Trans. Ind. Electron.*, vol. 67, no. 3, pp. 2430–2439, 2020.

[55] P. S. Addison, *The Illustrated Wavelet Transform Handbook Introductory Theory and Applications in Science, Engineering, Medicine and Finance*. CRC Press, 2016.

[56] W. van Drongelen, "Signal Processing for Neuroscientists Chapter 16 Wavelet Analysis: Frequency Domain Properties," in *Signal Processing for Neuroscientists: An Introduction to the Analysis of Physiological Signals*, 2007, pp. 265–277.

[57] J. B. Tary, R. H. Herrera, and M. Van Der Baan, "Analysis of time-varying signals using continuous wavelet and synchrosqueezed transforms," *Philos. Trans. R. Soc. A Math. Phys. Eng. Sci.*, vol. 376, no. 2126, 2018.

[58] C. Torrence and G. . Compo, "A practical guide to wavelet analysis," *Bull. Am. Meteorol. Soc.*, vol. 79, no. 1, pp. 61–78, 1998.

[59] D. Ainalis, L. Ducarne, O. Kaufmann, J. P. Tshibangu, O. Verlinden, and G. Kouroussis, "Improved blast vibration analysis using the wavelet transform," *24th Int. Congr. Sound Vib.*

View Article Online
DOI: 10.1039/D0NA00531B

ICSV 2017, 2017.

[60] S.C. Olhede and A.T. Walden, "Generalized Morse wavelets," *IEEE Trans. Signal Process.*, vol. 50, no. 11, pp. 2661–2670, 2002.

[61] J. M. Lilly and S. C. Olhede, "Generalized morse wavelets as a superfamily of analytic wavelets," *IEEE Trans. Signal Process.*, vol. 60, no. 11, pp. 6036–6041, 2012.

[62] S. S, "Performance evaluation of wavelet time-resolved phase-amplitude coupling estimates on small numbers of trials," *Interdiscip. Res. Rev.*, vol. 5, no. 1, pp. 1–8, 2020.

[63] J. M. Lilly and S. C. Olhede, "Higher-order properties of analytic wavelets," *IEEE Trans. Signal Process.*, vol. 57, no. 1, pp. 146–160, 2009.

[64] D. Maraun and J. Kurths, "Cross wavelet analysis: significance testing and pitfalls," *Nonlinear Process. Geophys.*, vol. 11, no. 4, pp. 505–514, 2004.

[65] A. Grinsted, J. C. Moore, and S. Jevrejeva, "Application of the cross wavelet transform and wavelet coherence to geophysical time series," *Nonlinear Process. Geophys.*, vol. 11, no. 4, pp. 515–533, 2004.

[66] C. Torrence and P. J. Webster, "Interdecadal changes in the ENSO-monsoon system," *J. Clim.*, vol. 12, no. 8 PART 2, pp. 2679–2690, 1999.

[67] A. F. Payam, "Dynamic modeling and sensitivity analysis of dAFM in the transient and steady state motions," *Ultramicroscopy*, vol. 169, pp. 55–61, 2016.

[68] A. F. Payam, J. R. Ramos, and R. Garcia, "Molecular and nanoscale compositional contrast of soft matter in liquid: Interplay between elastic and dissipative interactions," *ACS Nano*, vol. 6, no. 6, pp. 4663–4670, 2012.

[69] J. Melcher *et al.*, "Origins of phase contrast in the atomic force microscope in liquids," *Proc. Natl. Acad. Sci. U. S. A.*, vol. 106, no. 33, pp. 13655–13660, 2009.

[70] Y. T. Qassim, T. R. H. Cutmore, and D. D. Rowlands, "FPGA implementation of wavelet coherence for EEG and ERP signals," *Microprocess. Microsyst.*, vol. 51, pp. 356–365, 2017.

[71] Y. T. Qassim, T. R. H. Cutmore, and D. D. Rowlands, "Optimized FPGA based continuous wavelet transform," *Comput. Electr. Eng.*, vol. 49, pp. 84–94, 2016.

[72] S. Pradhan, "Real time identification of local surface properties of material using atomic force microscope - An FPGA based implementation," *Masters Thesis*, p. 66, 2017.

[73] R. García, J. Tamayo, M. Calleja, and F. García, "Phase contrast in tapping-mode scanning forcemicroscopy," *Appl. Phys. A Mater. Sci. Process.*, vol. 66, no. SUPPL. 1, pp. 309–312, 1998.

[74] N. F. Martínez and R. García, "Measuring phase shifts and energy dissipation with amplitude modulation atomic force microscopy," *Nanotechnology*, vol. 17, no. 7, pp. 167–172, 2006.

[75] H. Nagao, T. Uruma, K. Shimizu, N. Satoh, and K. Suizu, "Non-resonant frequency components observed in a dynamic Atomic Force Microscope," *Nonlinear Theory Its Appl. IEICE*, vol. 8, no. 2, pp. 118–128, 2017.

[76] S. Hornstein and O. Gottlieb, "Nonlinear multimode dynamics and internal resonances of the scan process in noncontacting atomic force microscopy," *J. Appl. Phys.*, vol. 112, no. 7, 2012.

[77] S. Dey and V. Kartik, "Intermittent impact dynamics of a cantilever scanning a surface at

high speed," *J. Appl. Phys.*, vol. 123, no. 12, 2018.

[78] M. Chiesa *et al.*, "Energy dissipation in the presence of sub-harmonic excitation in dynamic atomic force microscopy," *Epl*, vol. 99, no. 5, 2012.

[79] M. Chiesa *et al.*, "Investigation of nanoscale interactions by means of subharmonic excitation," *J. Phys. Chem. Lett.*, vol. 3, no. 16, pp. 2125–2129, 2012.

View Article Online
DOI: 10.1039/D0NA00531B